Ground-Penetrating Radar Detection and Three-Dimensional Mapping of Lateral Macropores: I. Calibration

Kevin H. Gormally
Marine, Estuarine, and Environ. Sci.
Univ. of Maryland
College Park, MD

currently at
The Johns Hopkins University Applied Physics Lab.
Laurel, MD

Marla S. McIntosh*
Plant Science and Landscape Architecture
Univ. of Maryland
College Park, MD

Anthony N. Mucciardi
TreeRadar, Inc.
Silver Spring, MD

Preferential flow of water through soil macropores is known to contribute to groundwater and surface water contamination as well as stream bank instability. However, research on the mechanisms and extent of soil macroporosity is limited due to the lack of a practical technique to study macropores in situ without disrupting the site's ecological function. In this paper, we present a ground-penetrating radar (GPR)-based methodology for detecting soil macropores smaller than 10 cm in diameter within 1 m of the soil surface and then creating a computerized tomogram of the macropore network. Manual and automated algorithms for macropore detection were tested for scan data collected using a 900-MHz radar antenna in a field experiment with a silt-loam soil. Buried polyvinyl chloride (PVC) pipes were used to simulate soil macropores of different diameters and fill contents intersected by GPR scan lines at four different angles. Pipes ≥ 3.00 cm in diameter were clearly detectable regardless of the scan line orientation relative to the target, and pipes with diameters as small as 1.85 cm were detected at perpendicular angles of intersection. In a second field experiment, PVC pipes of varying dimensions were buried at different depths to simulate a macropore network of preferential flow pathways. A branch-node algorithm was developed that referenced GPR scan line detections to create an accurate computer-generated three-dimensional map of the pipe network.

Abbreviations: 3-D, three-dimensional; CT, computed tomography; GPR, ground-penetrating radar; M^3A, Macropore Morphology Mapping Algorithm; PVC, polyvinyl chloride.

Recent studies have shown that lateral preferential flow through macropores can affect the nutrient buffering capabilities of riparian wetlands (Angier and McCarty, 2008) and play an important role in stream bank erosion (Fox and Wilson, 2010). However, our understanding of the prevalence and three-dimensional (3D) morphology of macropores in wetlands and hillsides near streams is limited by the challenge posed by in situ detection and mapping of these small pathways <10 cm diam.

There is a growing body of scientific literature detailing approaches and technologies for identifying subsurface hydrologic pathways. At a field scale, chemical tracers have been used to infer general riparian wetland flow patterns (Elçi and Molz, 2009; Kung et al., 2005) but not the specific channels of preferential flow. At a smaller scale, researchers in Japan have generated schematics and models of soil pipe networks < 10 cm in diameter from manual excavations with soil pits and fiberscope exploration (Sidle et al., 2000, 2001; Terajima et al., 2000). Colored dye tracing has proven useful for identifying vertical macropores in soil samples but requires destructive sampling (Morris and Mooney, 2004; Nobles et al., 2004; Pierret et al., 2002; Weiler, 2005). Chemical tracers have also been used to measure pore-size spectra in tile drain experiments (Kung et al., 2005). At a fine scale, computed tomography (CT) technology has been applied to construct high resolution imagery of interconnected micropore networks (approximately 1 mm in diameter) but requires destructive sampling of soils for laboratory analysis

Soil Sci. Soc. Am. J. 75:2011
Posted online 1June 2011
doi:10.2136/sssaj2010.339
Received 8 Sept. 2010.
*Corresponding author (mmcintos@umd.edu).

(Kettridge and Binley, 2008; Luo et al., 2008; Mooney and Korosak, 2009; Pierret et al., 2002; Quinton et al., 2009).

Ground-penetrating radar provides an alternate non-invasive approach for mapping groundwater flow pathways that can be conducted in the field over a relatively large area within a short time frame. Ground-penetrating radar can be used to find matrix discontinuities such as cavities with air or water by transmitting electromagnetic pulses into the ground and detecting the energy that reflects off those discontinuities due to a difference in electrical permittivity (k). The digitized waveforms of received reflections (A-scans) are assembled along a transect to form a two-dimensional profile of the subsurface (B-scan).

Low frequency GPR (25–100 MHz) has been used to map the stratigraphy of peats (peat/sand and peat/mineral interfaces) and generate general groundwater flow models but not pathways of preferential flow (Kettridge et al., 2008; Lowry et al., 2009). To that end, Holden (2004, 2005, 2006) and Holden et al. (2002) demonstrated applications of low frequency GPR sensors (100 and 200 MHz) to map networks of soil pipes larger than 10 cm in diameter in peats in the UK. Holden (2004) confirmed hydrologic linkages between the individual detections (i.e., created tomographs) by tracking the movement of salt tracers injected into the pipes. Holden et al. (2002) also conjectured that the methods based on low frequency sensors could be extended to detect soil pipes <10 cm in diameter by using a higher resolution antenna (>500 MHz) but there are no known published results.

In this paper, we demonstrate the potential of GPR-based algorithms to detect and automatically map 1- to 10-cm diam. macropore networks within the top meter of the soil. We used PVC pipes to model macropores and applied a 900-MHz antenna, the recommended frequency for applications targeting detections within 1 m. We describe a standard manual (i.e., operator-in-the-loop) detection procedure, a fully automated detection procedure, and a mapping algorithm based on CT methods that automatically connects detections into a 3D network of potential flow pathways. These three procedures were later applied and validated in a Mid-Atlantic riparian wetland (Gormally et al., 2011). As often as possible, the properties and conditions of this validation riparian site were replicated in the calibration field plots.

Similar calibration experiments have shown that experienced operators can use high frequency GPR sensors to detect pipe-like objects smaller than 10 cm in diameter. Both uniform linear targets such as utilities (Abu-Zreig et al., 2003; Allred et al., 2004; Park et al., 2003; Zarkhidze and Lemenager, 2004) and irregular structures such as tree roots (Barton and Montagu, 2004; Butnor et al., 2001; Cox et al., 2005; Hirano et al., 2009; Hruska and Cermak, 1999; Stover et al., 2007) were detectable within 1 m of the surface. Notably, Hirano et al. (2009) found that roots $\geq$ 1.9 cm in diameter were clearly detected in optimal sandy soil conditions in a laboratory experiment using a 900-MHz sensor.

These experiments relied on an experienced practitioner to analyze the GPR data but this restriction can potentially be overcome by using a computer algorithm to automatically detect reflection hyperbolas. Existing techniques range from simple counting, clustering, and Hough Transform-based algorithms (Capineri et al., 1998; Herman and Singh, 1995; Nagashima et al., 1995) to more robust approaches utilizing neural-network based image processing (Al-Nuaimy et al., 2002; Shihab et al., 2003; Youn and Chen, 2002) and scene analysis based on principle component analysis (Goldman and Cohen, 2004). Each of these methods offers unique insights into the problem of automated detection, but none appears to be a superior solution.

To predict the potential hydrologic connectivity between macropore detections, tracer-based techniques have been explored that result in a postulated preferential flow network. However, they are not practical for riparian macropore mapping applications. Holden (2004) verified soil pipe connectivity by injecting a salt water tracer with a pipette-like device into detected pore spaces and positioning the GPR sensor downstream to observe reflectance changes due to the salt. Besides the difficulty precisely intersecting smaller riparian channels with a pipette, it would be very time consuming to apply the salt water injection procedure to the large numbers of channels observed in the riparian wetland soils. Therefore, we propose a novel approach that automatically derives the network connections from the spatial distribution of the individual detections. To date, such methods have only been demonstrated for objects with simple linear geometries (Al-Nuaimy et al., 2002; Dell'Acqua et al., 2004; Shihab and Al-Nuaimy, 2005) or for objects that are much smaller than riparian channels (i.e., << 1 cm diam.) in optimal laboratory conditions using very high resolution scanning procedures developed for biomedical applications (e.g., CAT-scans) (Perret et al., 1999; Pierret et al., 2002; Wielopolski et al., 2002).

Here, we conducted two-field experiments using PVC pipes as a surrogate for macropores to calibrate and evaluate our GPR-based detection and mapping algorithms. In Exp. I, manual and automated detection procedures were evaluated using scan data from PVC pipes buried in native soil as targets simulating different sized macropores that were empty, partially empty, or full of water. The depths, shape, and diameters of the pipe targets were consistent with the macropores observed in soil cores by Angier et al. (2005) in a typical Mid-Atlantic riparian wetland as well as those observed on hillslopes (Sidle et al., 2001). The spatial resolution of the GPR sensor was bounded and detection performance was assessed for different scan line orientations. Scan line orientation is important for in situ application because soil macropores may be arrayed at a variety of angles to the GPR transect (Sidle et al., 2001), not solely perpendicular as assumed in other GPR research (Hirano et al., 2009). In Exp. II, a branch-node mapping algorithm was developed to connect GPR scan line pipe detections into a 3D prediction of their subsurface morphology. The algorithm was tested on a PVC pipe structure simulating schematics of preferential flow networks (Holden et al., 2002; Sidle et al., 2000, 2001; Terajima et al., 2000).

MATERIALS AND METHODS

Experiment I: Detection Calibration

Field Plot Layout

A 4 m by 3 m test plot was established at the University of Maryland Turfgrass Research and Education Facility in College Park, MD, in November 2007. The treatment design consisted of a 4 × 4 factorial combination of PVC pipes with different pipe diameters and fill types. The cavity diameters of the schedule 40 PVC pipes were 1.85, 3.00, 4.46, and 5.64 cm and each pipe contained either water, a 1:1 ratio of water and air, air, or salt water (22 mg cm^{-3} iodized sea salt). The 16 PVC pipes were arranged in a systematic design with pipe size as rows and fill type as columns (Fig. 1).

The soil was classified as a Keyport silt loam; a fine, mixed, semiactive, mesic Aquic Hapludult. This silt loam soil texture also occurs in nearby riparian wetlands. Thus, the detection medium in this study was a more realistic surrogate than sand used in a similar study (Hirano et al., 2009).

The PVC pipes were buried by removing the turfgrass and top soil and centering the pipes in trenches parallel to the ground surface at a depth of 16.0 ± 1.5 cm. Excavated soil was hand packed around each pipe to minimize the introduction of voids in the surrounding soil matrix. The turfgrass was then replaced and tamped down. The pipe length (91 cm) and distance between pipes (110 ± 7 cm) were chosen to avoid interactions with the leading edge of the GPR pulses.

The PVC pipes were used in the experiments because: (i) radar energy is almost completely transmitted through the PVC material given the radar's wavelength so only the pipe's contents should be detected; (ii) they are easily manipulated and available in many standard diameters; and (iii) their round shape is similar to that of the macropores observed in riparian wetlands (Angier and McCarty, 2008) and hillslopes (Terajima et al., 2000).

Ground-Penetrating Radar Data Collection

The GPR scan data were collected using a Geophysical Survey Systems Inc. portable TerraSIRch Subsurface Interface Radar system (SIR-3000, GSSI, Salem, NH) and a 900-MHz antenna. Transects for the GPR scan lines were spaced at 30-cm intervals and arranged at perpendicular, parallel, and 45° angles to the grid of buried pipes (Fig. 1). Propagation velocity was calibrated in situ by synchronizing the known depth of one of the buried pipes to the depth of the corresponding reflection observed on the system's A-scan display. Based on this calibration, the dielectric permittivity for the soil was measured to be 20 (consistent with a moist but not saturated soil), similar to $k = 24$ measured at the riparian validation site. It was assumed that there was little spatial variation in the soil water content and dielectric given the relatively small survey dimensions. The SIR-3000 computer also automatically set the four segments of a time-varying gain profile to compensate for the attenuation of the radar energy over depth.

The GPR system was manually propelled across the scan transects in a tricycle cart; the antenna was suspended underneath in a tub that rested on the ground. The radar system transmitted impulses into the ground at 5-mm intervals based on an optical encoder survey wheel. The actual pipe locations relative to the start of the scan line were recorded with the B-scan data as electronic markers each time the center of the antenna housing was directly above a pipe in the perpendicular and angled scan lines (in theory, the radar pulse projects directly downward from the center of the antenna), or at the end point of a pipe in the parallel scan lines.

Manual Detection Procedure

To locate the buried pipes, we first used a typical manual detection procedure that consisted of visually examining filtered B-scan data for the coherent echo-dynamic patterns of reflection hyperbolas. Echo-dynamics refer to the dynamics in amplitude and depth due to the elliptical footprint of the GPR wavefront that results in a classic "⋂" shape as shown in Fig. 2. The PVC pipe locations were predicted at the

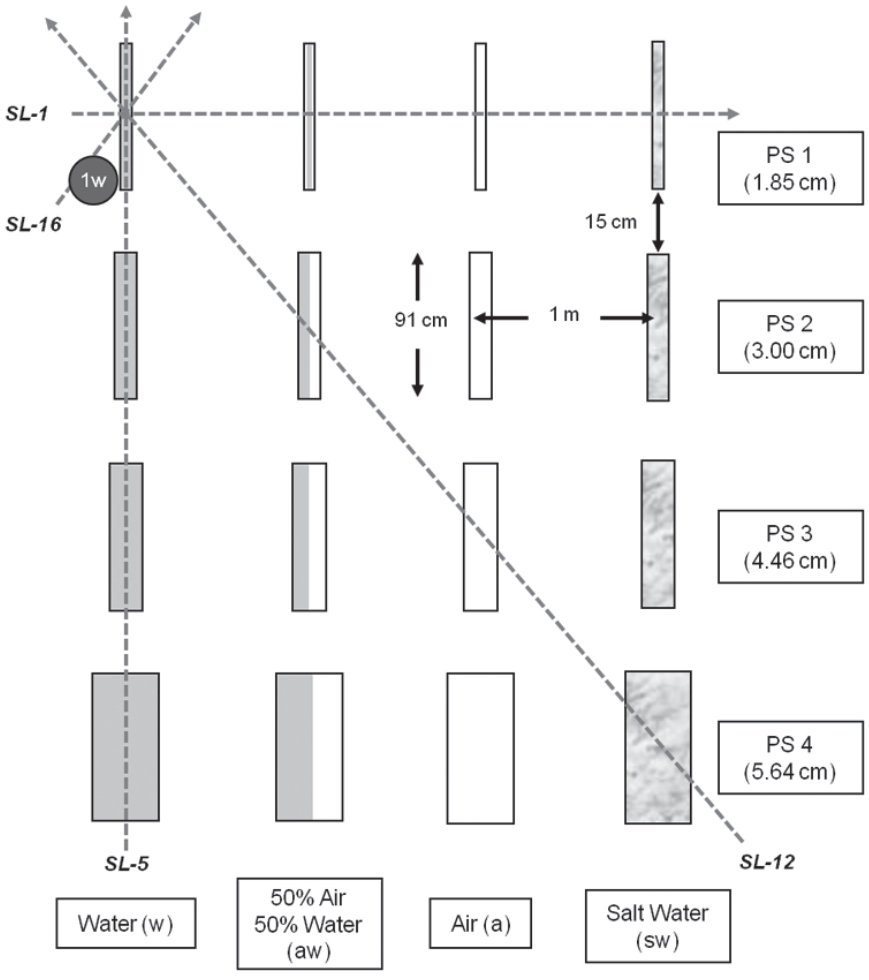

Fig. 1. Experiment I study plot layout with a factorial set of pipe size (PS, the inner pipe diameter) and fill type (w, aw, a, sw) treatments. Examples of each scan line orientation are shown as dashed lines intersecting pipe 1w: perpendicular intersection (SL-1), parallel intersection (SL-5), right-to-left angled intersection (SL-12), and left-to-right angled intersection (SL-16).

apex of the reflection hyperbola. Responses due to clutter sources were distinguished from targets by their relative lack of coherent dynamics and/or amplitude.

Software filters and visualization tools were created with the MATLAB software package (Ver. 7.3.0, The MathWorks, Natick, MA). A moving window average filter was used to enhance target reflections by removing constant bands of clutter energy out of small neighborhood windows (Annan, 2001; Conyers, 2004; Daniels, 2004).

The filter window length and detection threshold were set empirically during data analysis. The dimensionless rectified amplitude threshold was determined to be 6 based on measurements of the background amplitude values (mean = 1.4, SD = 1.7). A detection threshold can be determined for other sites by similarly measuring the recorded background amplitudes in data taken in those soils.

Automated Detection Procedure

A computerized detection algorithm was created to automatically isolate target reflections. A flow diagram of the algorithm and representative B-scan data are presented in Fig. 2. The process was modeled after the manual detection procedure. It conditions the raw B-scan input data to enhance the signal/noise ratio of the target reflections and then segments the data into regions of potential echo-dynamic patterns based on their form and amplitude.

The process is initialized with the moving window average prefilter. Boundaries of echo-dynamic response are isolated within an analysis depth range using a two-step hysteresis thresholding process similar to those used by Al-Nuaimy et al. (2002) and Shihab et al. (2003). First, pixels in the B-scan were found that exceeded the same rectified amplitude threshold level (6) used in the manual procedure. Then, these seed pixels were grouped with all neighboring pixels that exceeded a lower threshold (4.8) to form connected regions. Response regions were considered candidates for half-cycles of a target reflection provided that a minimum width requirement was satisfied (a distance along the scan that was set to eliminate spurious reflections) (Fig. 2a). The peak within the region is set as a centroid based on amplitude (Fig. 2b). Targets were predicted at locations where three alternating signed peaks (+/−/+ or −/+/−) were found within a window of depth (based on the sensor wavelength) and position (peaks should occur at a common position along the scan) (Fig. 2c).

Detection Accuracy Assessment

The performance of the manual and automated detection methodologies was assessed based on Type I and Type II error rates. These statistics were calculated from the numbers of correct (true) and incorrect (false) detections (positives) and dismissals (negatives) by comparing their locations to the actual pipe locations on a grid of position-depth cells. The area below 5 cm of each B-scan was divided into cells 22.9 cm long and 12.4 cm deep, which is the average area of the assumed reflection hyperbola response. Data corresponding to the upper 5 cm of soil was obscured by surface reverberation and were excluded from analysis.

A total of 1768 cells were evaluated, 64 of which contained targets. False positives (empty cells containing a mistaken detection) were counted as Type I errors. The Type I error rate was calculated as the percentage of empty cells containing false positives. Missed detections or false negatives (cells containing an undetected target) were counted as Type II errors. The Type II error rate was calculated as the percentage of cells containing true targets that were not detected. For each correct detection, a depth prediction error (D_e) was calculated as the difference between the predicted and actual pipe location in depth.

Experiment II: Mapping Calibration

Field Plot Layout

Experiment II was established in a 4 m by 3 m plot with the same soil classification as Exp. I. Air-filled PVC pipes were used to simulate both an extended macropore network as well as isolated macropore segments (Fig. 3). The network consisted of multiple bifurcating segments extending from a single source. The design of this model system was based on published descriptions of soil pipes observed on hillslopes. These studies show that macropores can vary in length with short segments that are approximately straight (Terajima et al., 2000) and have sudden starting and stopping characteristics (Holden et al., 2002; Sidle et al., 2000; Sidle et al., 2001; Terajima et al., 2000).

The pipe structure was created using schedule 40 pipes with diameters ranging from 1.85 to 5.64 cm. The segments were buried in trenches at depths between 8 and 33 cm and excavated soil was hand packed into the trenches around each pipe.

Ground-Penetrating Radar Data Collection and Detection Analysis

The GPR data were collected along parallel scan lines set perpendicular to the central axis of the pipe structure and intersected the pipes at various angles. The same system calibration settings were used as in Exp. I and the true pipe locations were recorded with electronic markers for subsequent analysis. The pipe reflections in the B-scan data were detected using the manual and the automated procedures described in Exp. I. Detection accuracy was assessed as described for Exp. I across 962 grid cells.

Mapping Algorithm

The morphology of the buried PVC pipe network was predicted using a branch-node connectivity algorithm that we created and refer to as the Macropore Morphology Mapping Algorithm (M^3A). A flow diagram of the steps in M^3A is given in Fig. 4. The M^3A uses a clustering and nearest neighbor reconstruction technique similar to that described by Perret et al. (1999). The algorithm connects detections from one scan line to the next by comparing their locations within the scan lines.

The M^3A was designed assuming that: (i) GPR data are collected along scan lines that form a discrete grid across the study area, (ii) the distance between scan lines provides adequate sampling of the subsurface morphology (as the spacing increases, the accuracy of the nearest neighbor associations decreases relative to the tortuosity of the structure), (iii) the detections from the scan analysis procedure correspond to the targeted subsurface structures (a low Type I error rate), and (iv) the scan analysis results in a nearly complete set of detections for the structure (low Type II error rate).

Detections on each scan line were considered sequentially to build the branch-node structure as depicted in Fig. 4. Potential

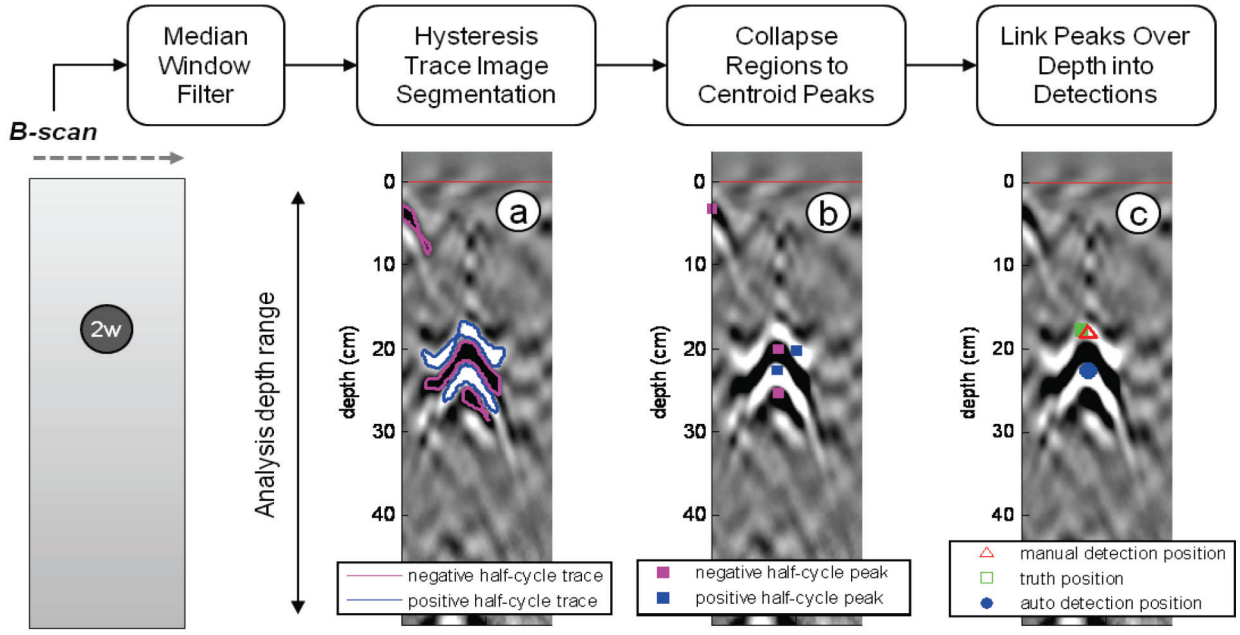

Fig. 2. Automated detection algorithm flow diagram and example application. Filtered B-scan data (centered on perpendicular intersection of water-filled 3.00 cm pipe) is given with (a) boundaries of positive and negative amplitude regions isolated by hysteresis thresholding, (b) centroid peak amplitude positions, and (c) automated detection compared to manual detection and truth target locations.

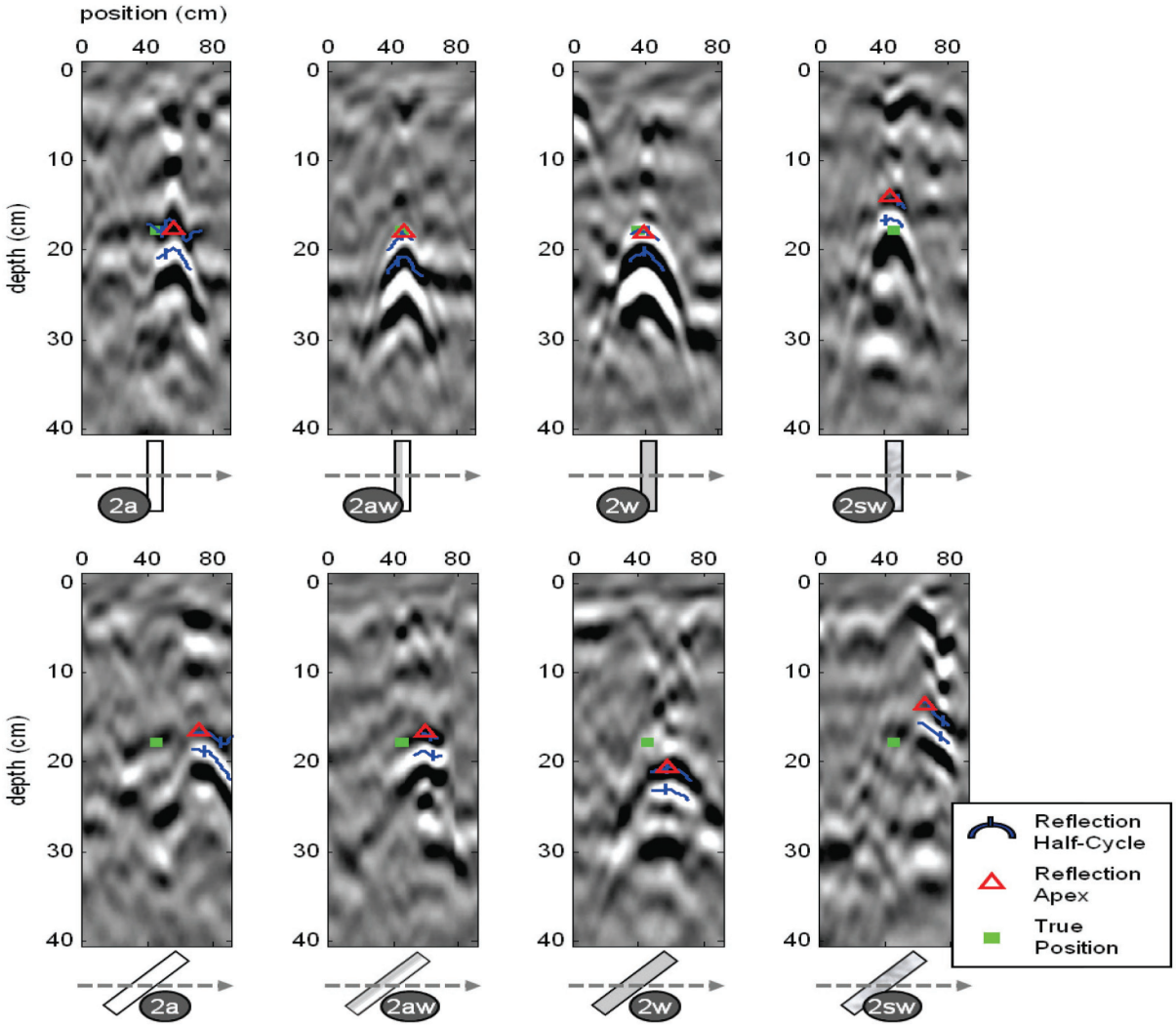

Fig. 5. Sample Exp. I B-scan data (90 cm long) for six intersections of the 3.00-cm diam. pipes: scan lines (top row) at perpendicular angles to the pipes, and (bottom row) at a 45° angle to the pipes.

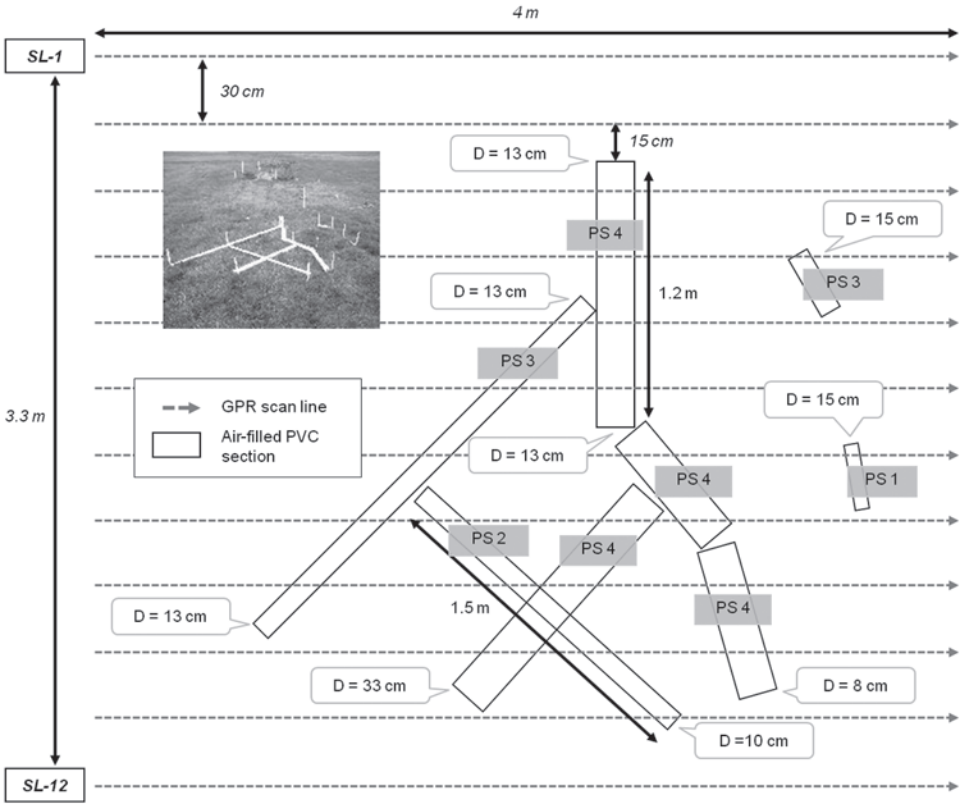

Fig. 3. Experiment II plot layout drawn to scale with pipe size (PS) and depth (D). Potential detections are points of intersection between the scan lines and the pipes.

matches of detections to existing branches were evaluated by checking whether the detection was within the extrapolations of those branches to the current scan line (association). If no match was found, a new branch was initialized with the detection (e.g., D1a) as the root node (initialization). If a match was found, the detection was connected as a node to that branch (smoothing; e.g., D1a → D2a). If multiple matches were found, the detection was connected to the branch with the best fit according to a nearest neighbor rule (adjudication). After all detections on the scan line were considered, extrapolation volumes were created on the next available scan line for all active branches. When the process finished considering data from all the scan lines, gaps between segments due to presumed false dismissals were closed (track coast). The connectivity links were then used in plotting functions to construct a visualization of the subsurface morphologies.

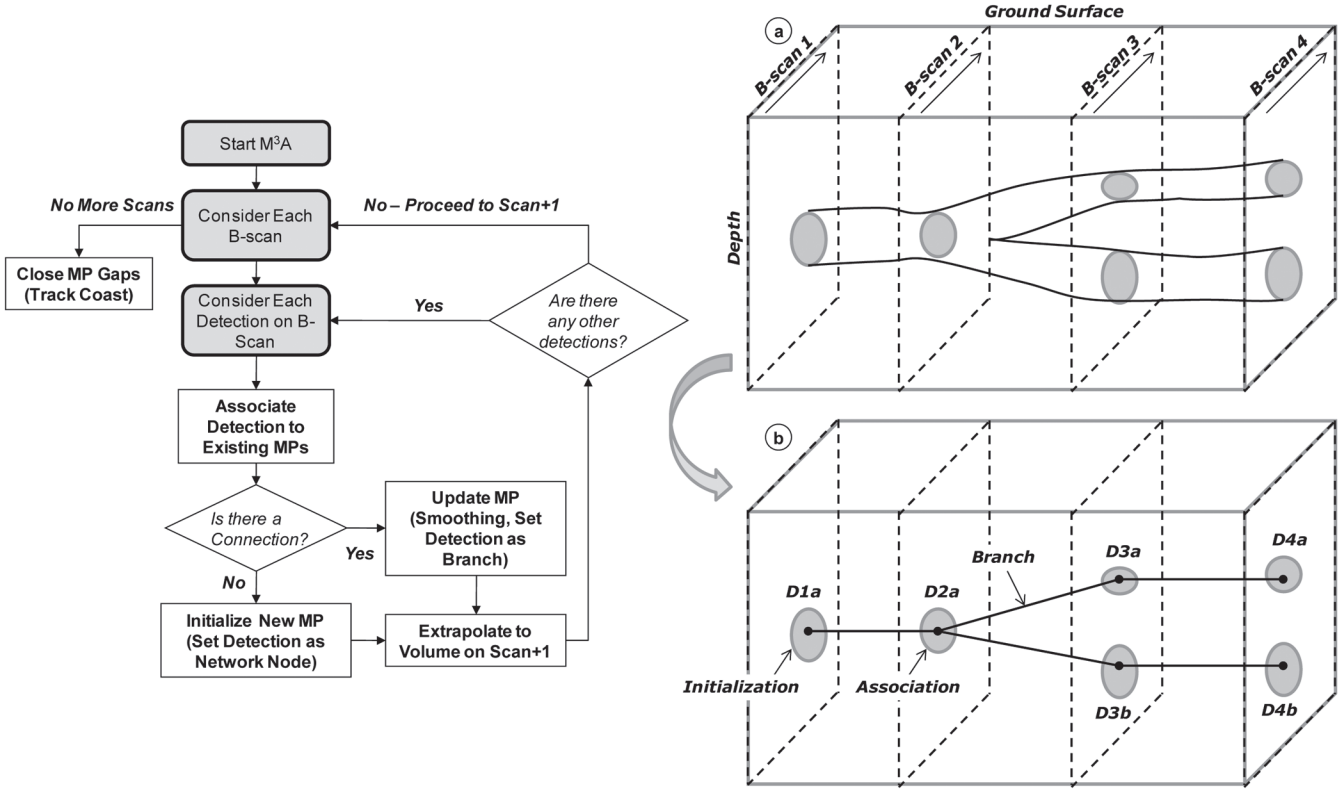

Fig. 4. Flow chart of the Macropore Morphology Mapping Algorithm (M^3A) and example application. (a) Schematic of a network intersected by four GPR B-scan lines, and (b) corresponding computed tomography result (MP). The branch-node map is initialized with detection *D1a* on scan line 1, one branch is associated on B-scan 2 (*D1a*→*D2a*), and two branches are associated on B-scan 3 *(D2a*→*{D3a, D3b}*) and continue on B-scan 4.

RESULTS AND DISCUSSION

Experiment I: Manual Detection Results

An experienced operator (K.H. Gormally) correctly detected 59 of the 64 total pipe intersections (16 pipes × 4 angles of intersection) using the manual detection methodology (Type II error rate = 7.8%), as summarized in Table 1. There were no false positives (Type I error rate = 0%).

Pipes ≥ 3.0 cm in diameter were detected regardless of the scan line orientation and fill type. The smallest pipes (1.85-cm diam.) were consistently detected in perpendicular and parallel scan line orientations. Hirano et al. (2009) similarly found that the lower diameter detection limit of pipe-like shapes with perpendicular scan lines was 1.9 cm using a 900-MHz antenna. The amplitudes of five of the eight reflections from 1.85-cm diam. pipes intersected at 45°angles were insufficient for detection. Correct detection of the 1.85-cm diam. pipes was dependent on whether the pipes were filled with air (100% detected), air + water (75% detected), or water (50% detected). This finding is consistent with the higher electromagnetic contrast (calculated as a ratio) between the soil media (k = 20) and air (k = 1), as compared with the contrast between the soil and water (k = 80).

The estimates of the depth of the pipes were generally accurate within 4 cm, or 54% of the wavelength at the antenna's center frequency (mean D_e = −0.6 cm, SD = 1.8 cm). This is comparable with the depth estimation accuracy reported by Holden et al. (2002) for a 200-MHz antenna: ± 30 cm, or approximately 60% of that sensor's wavelength.

Example B-scan data is shown in Fig. 5. Reflection differences from different fill contents and angles of intersection are apparent. The amplitude of the reflected energy (not shown in figure) generally increased with the pipe diameter as expected.

Experiment I: Automated Detection Results

The automated detection algorithm had a nominal Type I error rate (0.5%) that was comparable with the manual procedure but at a lower detection rate (77.3%) (Table 1). As with the manual procedure, most of the missed detections were due to the lower amplitude reflections from the smallest pipes. The detection rate was 87% for intersections with pipes ≥ 3.0 cm in diameter compared with 31% for the 1.85 cm pipe intersections. Differences in the detection rate of pipes ≥ 3.0 cm were found between intersection angles (perpendicular and parallel = 96%; angled = 79%) and fill types (air = air + water = 92%; water = 75%). Depth prediction errors matched those of the manual procedure.

Experiment II: Detection Results

The Exp. II detection results are given in Table 1. The 12 scan lines crossed the buried pipes 22 times. All 22 intersections were manually detected with no false positives (Fig. 6a). As in Exp. I, the median depth error was near zero. Depth estimates were generally accurate within 2 cm (27% of the wavelength at the antenna center frequency). The automated procedure had two false positives and five missed detections, including both of the intersections with the short unconnected pipe segments (Fig. 6b). The missed detections were due to lower amplitude reflections from angled scan line intersections as well as an inability to distinguish the splitting pipes on SL-5 (one of the three such cases in which two pipe intersections were closely located along a B-scan). For pipes ≥ 3.00 cm in diameter, the detection rate was 81%.

Experiment II: Mapping Results

Based on the set of manual detections, the mapping algorithm correctly predicted that three separate macropore structures were present in the subsurface (Fig. 6a). The M^3A mapping of the connected pipe network robustly tracked the structure's bifurcations and changes in direction across scan lines. The two unconnected pipe segments were each mapped with a single node. Thus, M^3A accurately concluded that the short segments did not span multiple scan lines. The maps were also rendered in 3D as shown in Fig. 7.

The mapping predictions resulting from the set of automated detections were somewhat less accurate than those based on the manual detections. Because the automated procedure did not detect either of the unconnected segments, these pipes were not mapped by M^3A. The other three false negatives and two false positives resulted in segment deviations and an additional node (Fig. 6b). However, the mapping still closely resembled the truth layout, including the bifurcations and changes in direction, because the M^3A track coast function closed the gaps between detections.

SUMMARY AND CONCLUSIONS

A manual GPR detection procedure was used to effectively locate PVC pipe targets simulating preferential flow channels with diameters from 1.85 to 5.64 cm at depths from 8 to 33 cm

Table 1. Manual and automated detection performance metrics for grid cells defined in a depth range below 5 cm in Exp. I (22 B-scans) and Exp. II (12 B-scans).

	Exp. I †		Exp. II ‡	
Detection performance metric	Manual procedure	Automated procedure	Manual procedure	Automated procedure
Accurate detections (pt)	59	47	22	17
Empty grid cells predicted empty (nc)	1704	1696	938	936
False positives, Type I Errors (pc)	0	8	0	2
Missed detections, Type II Errors (nt)	5	17	0	5
Type I Error rate (pc/c)	0%	0.5%	0%	0.2%
Type II Error rate (nt/t)	7.8%	26.6%	0%	22.7%

† Total grid cells (t+c) = 1768, Potential detections (t) = 64, Cells not containing truth (c) = 1704.

‡ Total grid cells (t+c) = 962, Potential detections (t) = 22, Cells not containing truth (c) = 938.

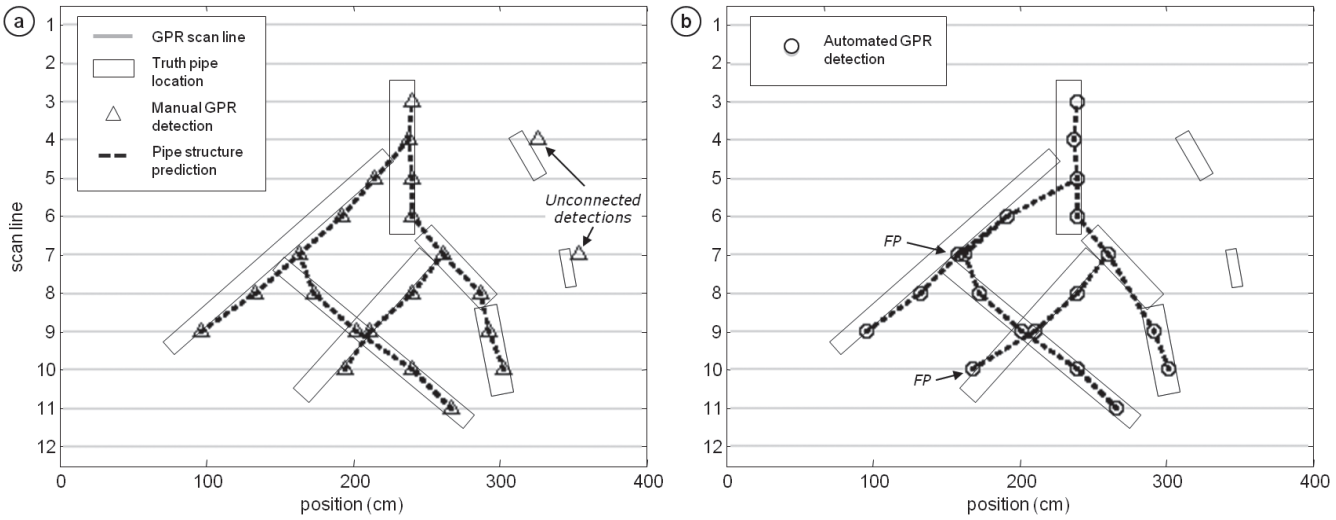

Fig. 6. Top-down view of the (a) manual and (b) automated Exp. II pipe structure predictions compared to the truth layout. FP = false positive detection.

in a silt loam soil. Across two experiments, the manual procedure had a detection rate > 92% and no false positives. The minimum resolvable object size depended on the angle of intersection. For perpendicular scan line intersections, pipes ≥ 1.85 cm in diameter were reliably detected. For angled scan line intersections, the smallest consistently detected pipe diameter was 3.00 cm. This affirms the importance of establishing GPR scan line grids normal to the orientation of the subsurface targets. Depth errors were a fraction of the sensor's wavelength, as expected.

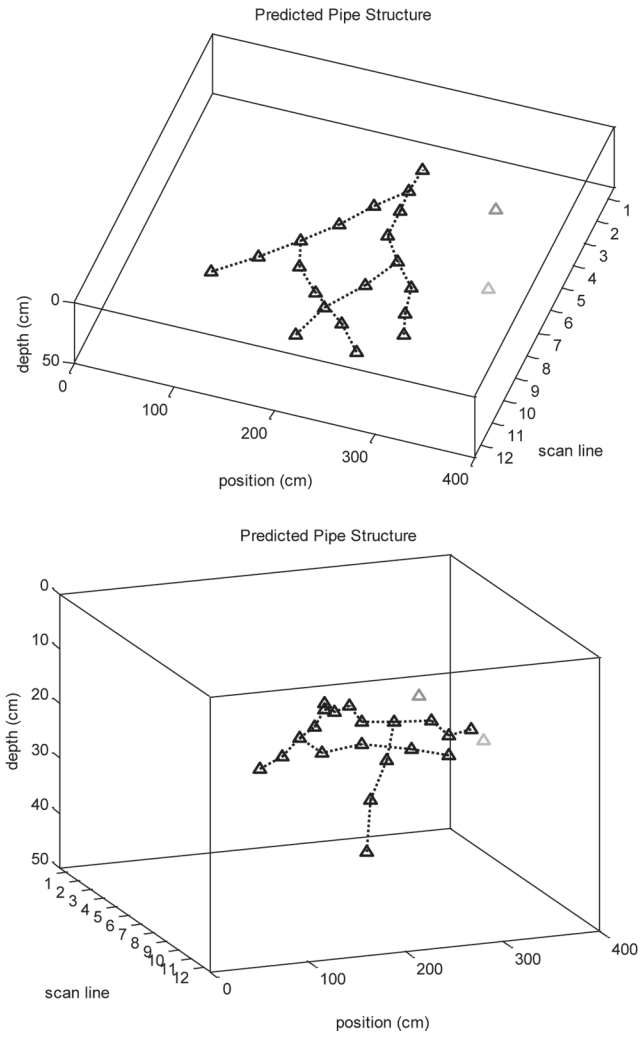

Fig. 7. Two 3D views of the predicted Exp. II layout based on the manual procedure detections.

Our automated detection procedure successfully detected > 77% of the experiment targets at a similar Type I error rate as the manual procedure. Although the Type II error rate was higher than the outcome from the human operator, utilizing the computer algorithm has the distinct advantage of consistently generating detections at the speed of a computer's processor without performance degradation due to analyst fatigue. The benefits of both approaches could be realized by using the algorithm as a preprocessing routine to bootstrap the results of a subsequent manual detection analysis. We recommend additional research and development to decrease the detection performance gap, particularly for low amplitude reflections and targets in close proximity along a B-scan. The algorithm could be improved by employing adaptive amplitude thresholding techniques based on amplitude histograms (Shen et al., 2004), more robust segmentation techniques (Malik et al., 2001; Svensson, 2008), or an iterative methodology (Dell'Acqua et al., 2004; Goldman and Cohen, 2004).

Additional study is also recommended to determine the applicability of the manual and automated procedures to targets and soils with different properties than those considered here. For example, the procedures may not directly apply to hillslope detection where most macropores have been found to be <3.0 cm (Sidle et al., 2001). A higher frequency antenna, a more sensitive detection threshold, and/or different preprocessing filter settings may be required to resolve these smaller pore spaces.

The results of Exp. II demonstrated the feasibility of referencing a set of detections to automatically map the morphology of channel-like objects in the subsurface. Using both the manual and automated procedure detections, our 3D branch-node algorithm, M^{3}A, robustly mapped a PVC

pipe structure simulating a macropore network. Short isolated macropores were manually detected if intersected by a scan line, but the mapping resolution was limited by the scan line spacing. To better resolve these smaller structures, additional more closely spaced scan line data could be collected and analyzed.

These experiments demonstrate the power of GPR detection and mapping algorithms as tools for non-invasively uncovering the potential pathways of by-pass flow in riparian areas. The procedures developed and tested here are an initial step toward advancing our understanding of preferential flow and contaminant fate. A companion paper (Gormally et al., 2011) demonstrates the application of these procedures and validates their effectiveness within an actual Mid-Atlantic riparian wetland.

ACKNOWLEDGMENTS

The authors acknowledge and thank David Funk for his assistance creating the study plots. We also gratefully acknowledge Gregory McCarty, David Tilley, and Claire Welty for their technical consultation, and the SSSAJ reviewers who greatly enhanced this paper with their many constructive comments.

REFERENCES

Abu-Zreig, M., R.P. Rudra, H.R. Whiteley, M.N. Lalonde, and N.K. Kaushik. 2003. Phosphorus removal in vegetated filter strips. J. Environ. Qual. 32:613–619. doi:10.2134/jeq2003.0613

Allred, B.J., N.R. Fausey, C. Chen, and L. Peters. 2004. GPR detection of drainage pipes in farmlands. p. 307–310. *In* Proc. Int. Conf. on Ground Penetrating Radar, 10th, June 2004, Delft, The Netherlands.

Al-Nuaimy, W., H. Lu, and S. Shihab. 2002. Automatic target detection in GPR data. p. 139–143. *In* S. Koppenjan and L. Hua (ed.) Proc. Int. Conf. on Ground Penetrating Radar, 9th, May 2002, Santa Barbara, CA.

Angier, J.T., and G.W. McCarty. 2008. Variations in base-flow nitrate flux in a first-order stream and riparian zone. J. Am. Water Resour. Assoc. 44:367–380. doi:10.1111/j.1752-1688.2007.00153.x

Angier, J.T., G.W. McCarty, and K.L. Prestegaard. 2005. Hydrology of a first-order riparian zone and stream, Mid-Atlantic coastal plain, Maryland. J. Hydrol. 309:149–166. doi:10.1016/j.jhydrol.2004.11.017

Annan, A.P. 2001. Ground penetrating radar workshop notes. Sensors & Software, Mississauga, ON, Canada.

Barton, C., and K. Montagu. 2004. Detection of tree roots and determination of root diameters by ground penetrating radar under optimal conditions. Tree Physiol. 24:1323–1331.

Butnor, J.R., J.A. Doolittle, L. Kress, S. Cohen, and K.H. Johnsen. 2001. Use of ground-penetrating radar to study tree roots in the southeastern United States. Tree Physiol. 21:1269–1278.

Capineri, L., P. Grande, and J.A.G. Temple. 1998. Advanced image-processing technique for real-time interpretation of ground-penetrating radar images. Int. J. Imaging Syst. Technol. 9:51–59. doi:10.1002/(SICI)1098-1098(1998)9:1<51::AID-IMA7>3.0.CO;2-Q

Conyers, L.B. 2004. Ground-penetrating radar for archaeology. AltaMira Press, Walnut Creek, CA.

Cox, K.D., H. Scherm, and N. Serman. 2005. Ground-penetrating radar to detect and quantify residual root fragments following peach orchard clearing. Horttechnology 15:600–607.

Daniels, D.J. 2004. Ground penetrating radar. Institution of Electrical Engineers, London.

Dell'Acqua, A., A. Sarti, S. Tubaro, and L. Zanzi. 2004. Detection of linear objects in GPR data. Signal Process. 84:785–799. doi:10.1016/j.sigpro.2003.12.010

Elçi, A., and F.J. Molz. 2009. Identification of lateral macropore flow in a forested riparian wetland through numerical simulation of a subsurface tracer experiment. Water Air Soil Pollut. 197:149–164. doi:10.1007/s11270-008-9798-5

Fox, G.A., and G.V. Wilson. 2010. The role of subsurface flow in hillslope and stream bank erosion. Soil Sci. Soc. Am. J. 74:717–733. doi:10.2136/sssaj2009.0319

Goldman, A., and I. Cohen. 2004. Anomaly detection based on an iterative local statistics approach. Signal Process. 84:1225–1229. doi:10.1016/j.sigpro.2004.04.004

Gormally, K.H., M.S. McIntosh, A.N. Mucciardi, and G.W. McCarty. 2011. Ground-penetrating radar detection and three-dimensional mapping of lateral macropores: II. Riparian application. Soil Sci. Soc. Am. J. 75: (this issue).

Herman, H., and S. Singh. 1995. First results in autonomous retrieval of buried objects. Autom. Construct. 4:111–123. doi:10.1016/0926-5805(94)00038-O

Hirano, Y., M. Dannoura, K. Aono, T. Igarashi, M. Ishii, K. Yamase, N. Makita, and Y. Kanazawa. 2009. Limiting factors in the detection of tree roots using ground-penetrating radar. Plant Soil 319:15–24. doi:10.1007/s11104-008-9845-4

Holden, J. 2006. Sediment and particulate carbon removal by pipe erosion increase over time in blanket peatlands as a consequence of land drainage. J. Geophys. Res. 111:F02010. doi:10.1029/2005JF000386

Holden, J. 2005. Controls of soil pipe frequency in upland blanket peat. J. Geophys. Res. 110:F01002. doi:10.1029/2004JF000143

Holden, J. 2004. Hydrological connectivity of soil pipes determined by ground-penetrating radar tracer detection. Earth Surf. Processes Landforms 29:437–442. doi:10.1002/esp.1039

Holden, J., T.P. Burt, and M. Vilas. 2002. Application of ground-penetrating radar to the identification of subsurface piping in blanket peat. Earth Surf. Processes Landforms 27:235–249. doi:10.1002/esp.316

Hruska, J., and J. Cermak. 1999. Mapping tree root systems with ground-penetrating radar. Tree Physiol. 19:125–130.

Kettridge, N., and A. Binley. 2008. X-ray computed tomography of peat soils: Measuring gas content and peat structure. Hydrol. Processes 22:4827–4837. doi:10.1002/hyp.7097

Kettridge, N., X. Comas, A. Baird, L. Slater, M. Strack, D. Thompson, H. Jol, and A. Binley. 2008. Ecohydrologically important subsurface structures in peatlands revealed by ground-penetrating radar and complex conductivity surveys. J. Geophys. Res. 113:G04030. doi:10.1029/2008JG000787

Kung, K.J.S., M. Hanke, C.S. Helling, E.J. Kladivko, T.J. Gish, T.S. Steenhuis, and D.B. Jaynes. 2005. Quantifying pore-size spectrum of macropore-type preferential pathways. Soil Sci. Soc. Am. J. 69:1196–1208. doi:10.2136/sssaj2004.0208

Lowry, C.S., D. Fratta, and M.P. Anderson. 2009. Ground penetrating radar and spring formation in a groundwater dominated peat wetland. J. Hydrol. 373:68–79. doi:10.1016/j.jhydrol.2009.04.023

Luo, L., H. Lin, and P. Halleck. 2008. Quantifying soil structure and preferential flow in intact soil using x-ray computed tomography. Soil Sci. Soc. Am. J. 72:1058–1069. doi:10.2136/sssaj2007.0179

Malik, J., S. Belongie, T. Leung, and J. Shi. 2001. Contour and texture analysis for image segmentation. Int. J. Comput. Vis. 43:7–27. doi:10.1023/A:1011174803800

Mooney, S.J., and D. Korosak. 2009. Using complex networks to model two- and three-dimensional soil porous architecture. Soil Sci. Soc. Am. J. 73:1094–1100. doi:10.2136/sssaj2008.0222

Morris, C., and S.J. Mooney. 2004. A high-resolution system for the quantification of preferential flow in undisturbed soil using observations of tracers. Geoderma 118:133–143. doi:10.1016/S0016-7061(03)00189-7

Nagashima, Y., H. Saito, S. Kobayashi, and J. Masuda. 1995. Automatic recognition of hyperbolic patterns in underground cross-sectional images. p. 953–956. *In* Proc. Symp. Application Geophysics to Eng. and Environ. Problems. 23–26 Apr. 1995, Orlando, FL.

Nobles, M.M., L.P. Wilding, and K.J. Mclnnes. 2004. Pathways of dye tracer movement through structured soils on a macroscopic scale. Soil Sci. 169:229–242. doi:10.1097/01.ss.0000126838.81093.20

Park, Y., K. Kim, S. Cho, D. Yoo, D. Youn, and Y. Jeong. 2003. Development of a UWB GPR system for detecting small objects buried under ground. p. 384–388. *In* IEEE Conf. Ultra Wideband Sys. and Tech., 16–19 Nov. 2003.

Perret, J., S.O. Prasher, A. Kantzas, and C. Langford. 1999. Three-dimensional quantification of macropore networks in undisturbed soil cores. Soil Sci. Soc. Am. J. 63:1530–1543. doi:10.2136/sssaj1999.6361530x

Pierret, A., Y. Capowiez, L. Belzunces, and C.J. Moran. 2002. 3D reconstruction and quantification of macropores using x-ray computed tomography and image analysis. Geoderma 106:247–271. doi:10.1016/S0016-7061(01)00127-6

Quinton, W.L., T. Elliot, J.S. Price, F. Rezanezhad, and R. Heck. 2009. Measuring

physical and hydraulic properties of peat from x-ray tomography. Geoderma 153:269–277. doi:10.1016/j.geoderma.2009.08.010

Shen, Y., C. Shu-zhen, and Z. Bing. 2004. An improved double-threshold method based on gradient histogram. Wuhan Univ. J. Nat. Sci. 9:473–476. doi:10.1007/BF02830446

Shihab, S., and W. Al-Nuaimy. 2005. Data fusion for accurate detection of pipe geometry using GPR. p. 99–102. *In* Proc. Int. Workshop on Advanced Ground Penetrating Radar, 3rd. 2005.

Shihab, S., W. Al-Nuaimy, Y. Huang, and A. Eriksen. 2003. A comparison of segmentation techniques for target extraction in ground penetrating radar data. p. 95–100. *In* Proc. Int. Workshop on Adv. Ground Penetrating Radar, 2nd, 14–16 May 2003. Delft, The Netherlands.

Sidle, R.C., S. Noguchi, Y. Tsuboyama, and K. Laursen. 2001. A conceptual model of preferential flow systems in forested hillslopes: Evidence of self-organization. Hydrol. Processes 15:1675–1692. doi:10.1002/hyp.233

Sidle, R.C., Y. Tsuboyama, S. Noguchi, I. Hosoda, M. Fujieda, and T. Shimizu. 2000. Stormflow generation in steep forested headwaters: A linked hydrogeomorphic paradigm. Hydrol. Processes 14:369–385. doi:10.1002/(SICI)1099-1085(20000228)14:3<369::AID-HYP943>3.0.CO;2-P

Stover, D., F. Day, J.R. Butnor, and B.G. Drake. 2007. Effect of elevated CO_2 on coarse-root biomass in Florida scrub detected by ground-penetrating radar. Ecology 88:1328–1334. doi:10.1890/06-0989

Svensson, S. 2008. Aspects on the reverse fuzzy distance transform. Pattern Recognit. Lett. 29:888–896. doi:10.1016/j.patrec.2008.01.006

Terajima, T., T. Sakamoto, and T. Shirai. 2000. Morphology, structure and flow phases in soil pipes developing in forested hillslopes underlain by a quaternary sand-gravel formation, Hokkaido, northern main island in Japan. Hydrol. Processes 14:713–726. doi:10.1002/(SICI)1099-1085(200003)14:4<713::AID-HYP968>3.0.CO;2-T

Weiler, M. 2005. An infiltration model based on flow variability in macropores: Development, sensitivity analysis and applications. J. Hydrol. 310:294–315. doi:10.1016/j.jhydrol.2005.01.010

Wielopolski, L., G. Hendrey, J. Daniels, and M. McGuigan. 2002. Imaging tree root systems in situ. p. 58–62. *In* S. Koppenjan and L. Hua (ed.) Proc. Int. Conf. on Ground Penetrating Radar, 9th, May 2002, Santa Barbara, CA.

Youn, H., and C. Chen. 2002. Automatic GPR target detection and clutter reduction using neural network. p. 579–582. *In* S. Koppenjan and L. Hua (ed.) Proc. Int. Conf. on Ground Penetrating Radar, 9th, May 2002, Santa Barbara, CA.

Zarkhidze, A., and E. Lemenager. 2004. Case study—Use of 3D GPR technologies for utility mapping in Paris. p. 375–378. *In* Proc. Int. Conf. on Ground Penetrating Radar, 10th, June 2004, Delft, The Netherlands.